Micromechanical modeling of the work-hardening behavior of single- and dual-phase steels under two-stage loading paths

Kengo Yoshida, Renald Brenner, Brigitte Bacroix, Salima Bouvier

Micromechanical modeling of the work-hardening behavior of single- and dual-phase steels under two-stage loading paths

Kengo Yoshida [a,b,*], Renald Brenner [a], Brigitte Bacroix [a], Salima Bouvier [a]

[a] *LPMTM, CNRS, University Paris 13, 99 Avenue Jean-Baptiste Clement, 93430 Villetaneuse, France*

[b] *Forming Technologies R&D Center, Steel Research Laboratories, Nippon Steel Corporation, 20-1 Shintomi, Futtsu, Chiba 293-8511, Japan*

Work-hardening behavior of single-phase steel and dual-phase steel which is made of hard martensite surrounded by soft ferrite is analyzed by using an elastoplastic crystal plasticity model in conjunction with the incremental self-consistent model. Two-stage loading paths consisting of uniaxial tension, unloading and subsequent uniaxial tension/compression for various directions are applied. Bauschinger effect and transitional re-yielding behavior, which depends on the direction of the second loading path, are pre-dicted and analyzed with respect to the distribution of the residual resolved shear stresses within the material. These features, which are caused by the inhomogeneity of the residual stress field, are especially pronounced in the case of the dual-phase steel because of the strong mechanical contrast between ferrite and martensite phases.

1. Introduction

In the context of metal forming processes, a sheet metal undergoes complex strain paths. In the last decades, intensive experimental works have been carried out to understand the deformation behavior of low carbon and IF steels under complex strain paths. In some of the studies [1–3] various two-stage strain paths were applied to sheet samples and the mechanical behavior and dislocation substructures were observed. A lower re-yield stress with work-hardening stagnation was observed under the reverse loading path (i.e. the directions of strain increment in the first and second paths are opposite). An increase of the re-yield stress followed by work softening was detected under the orthogonal loading path (i.e. the contracted product of the strain increments in the first and second path is zero). These behaviors are often called as the Bauschinger and cross-hardening effects, respectively. Based on TEM observations, these mechanical behaviors were correlated to dislocation substructures. When the loading is reversed, dislocation cell structure dissolves and mobile dislocations annihilate with the dislocations with the opposite sign. Consequently, the re-yield stress is lowered. The cross-hardening effect is caused by dislocation cells walls formed parallel to the active slip systems in the first loading, which becomes obstacles to mobile dislocations on new active slip systems during the second loading. The work-hardening behavior of IF steel is now well recognized in terms of the dislocation substructure.

Unlike IF and mild steels, there have been fewer studies on the plastic deformation behavior of dual-phase steel under complex loading paths. In some of the experimental works [4–8] complex loading paths were applied to dual-phase steels, and it was observed that in the reverse loading path, the stress–strain curve during unloading deviates from the one estimated by the Hooke's law, and large Bauschinger effect and permanent softening were observed. The Bauschinger effect is more pronounced for the dual-phase steel than for IF steel. In the work of Haddadi et al. [6] and Gardey et al. [4], the orthogonal loading path is applied to a dual-phase steel and they revealed that almost no cross-hardening effect takes place for the material, which is clear difference from the IF/mild steels. Following the traditional approach, Gardey et al. [4] observed dislocation substructure by means of TEM and found that the dislocation cell structures were more difficult to form and to dissolve in dual-phase steel than in IF steel. However, there is quite a difference in the formation of dislocation cell structures and this observation cannot explain the different mechanical behaviors observed in the two kinds of steels. Unlike IF steel, there is no clear one to one correlation between dislocation substructure and work-hardening behavior.

The two following mechanisms could explain the difference in the work-hardening behavior: (i) martensite is formed by displacive transformation so that internal residual stresses can exist

* Corresponding author. Present address: Graduate School of Science and Engineering, Yamagata University, 4-3-16 Jonan, Yonezawa, Yamagata, 992-8510 Japan. Tel.: +81 238 26 3217; fax: +81 238 26 3205.

E-mail address: yoshida@yz.yamagata-u.ac.jp (K. Yoshida).

within the material at the initial state, and/or (ii) the mechanical contrast between ferrite and martensite leads to a highly heterogeneous stress field. From the latter point of view, the Bauschinger effect was numerically studied by Zhonghua and Haicheng [9] for a dual-phase steel and by Terada et al. [10] for a ferrite–cementite two-phase material, for instance. In both studies, two-dimensional finite elements model consisting of hard phase surrounded by soft phase is constructed, and uniaxial tension followed by uniaxial compression was considered in [9] while plane strain tension followed by plane strain compression was applied in [10]. They reported that the heterogeneous stress field derives the Bauschinger effect. In these works, however, isotropic phenomenological constitutive model was adopted so that the heterogeneity among grains was neglected. Furthermore the work-hardening behavior was investigated only for the tension–compression loading.

The present investigation is an attempt to capture the influence of stress and strain heterogeneities within the polycrystal on the work-hardening behavior under complex loading paths. The mechanical behavior of single- and dual-phase steel is estimated by means of homogenization techniques in the framework of crystalline plasticity. To give an insight into the sole influence of the stress heterogeneity, other mechanisms which contribute to Bauschinger and cross-hardening effects are neglected. For instance, initial residual stresses are not considered, the slip systems are assumed to harden isotropically while texture evolution is neglected. The brief outline of the paper is as follows. In Section 2, a rate-independent crystal plasticity model and the Hill's incremental self-consistent model [11], which is one of the most customary approaches, are briefly reviewed. In Section 3, two-stage loading paths and material properties used in simulation are given. For comparison, in addition to a dual-phase steel, a single-phase steel the strength of which is almost the same as the dual-phase steel is also considered. In Section 4, the heterogeneity within single-phase steel, which emerges due to the crystalline anisotropy of the grains, is investigated first. Then, in Section 5, the work-hardening behavior of dual-phase steel is studied.

2. Theoretical frameworks

2.1. Rate-independent crystal plasticity model

In this study, we use the crystal plasticity formulation described in [12,13]. We confine attention to small strain conditions. The strain rate is given by the symmetry part of $\partial \mathbf{v}/\partial \mathbf{x}$, where $\mathbf{v}$ and $\mathbf{x}$ are velocity and position, respectively. We consider additive decomposition of strain rate into elastic and plastic parts.

$$\dot{\boldsymbol{\varepsilon}} = \dot{\boldsymbol{\varepsilon}}^{\mathrm{e}} + \dot{\boldsymbol{\varepsilon}}^{\mathrm{p}}. \tag{1}$$

Elastic relation is given by Hooke's law.

$$\dot{\boldsymbol{\sigma}} = \mathbf{C}^{\mathrm{e}} : \dot{\boldsymbol{\varepsilon}}^{\mathrm{e}} = \mathbf{C}^{\mathrm{e}} : (\dot{\boldsymbol{\varepsilon}} - \dot{\boldsymbol{\varepsilon}}^{\mathrm{p}}), \tag{2}$$

where $\boldsymbol{\sigma}$ and $\mathbf{C}^{\mathrm{e}}$ are the true stress and the forth-order elastic moduli tensor, respectively.

Crystallographic slips are considered to be the source for the plastic deformation, and the plastic strain rate takes the form

$$\dot{\boldsymbol{\varepsilon}}^{\mathrm{p}} = \sum_{\alpha} sgn(\tau^{(\alpha)})\dot{\gamma}^{(\alpha)}\mathbf{p}^{(\alpha)}, \tag{3}$$

$$\mathbf{p}^{(\alpha)} := \tfrac{1}{2}(\mathbf{s}^{(\alpha)} \otimes \mathbf{m}^{(\alpha)} + \mathbf{m}^{(\alpha)} \otimes \mathbf{s}^{(\alpha)}), \tag{4}$$

where $\dot{\gamma}^{(\alpha)}$, $\mathbf{s}^{(\alpha)}$, and $\mathbf{m}^{(\alpha)}$ are the positive slip rate, the slip direction and the slip plane normal for the αth slip system, respectively.

Based on the Schmid law, the yield function is written as

$$f^{(\alpha)} = |\tau^{(\alpha)}| - g^{(\alpha)} = 0, \tag{5}$$

where the resolved shear stress for the αth slip system, $\tau^{(\alpha)}$, is given as

$$\tau^{(\alpha)} = \mathbf{s}^{(\alpha)} \cdot \boldsymbol{\sigma} \cdot \mathbf{m}^{(\alpha)} = \boldsymbol{\sigma} : \mathbf{p}^{(\alpha)} \tag{6}$$

Based on yield function, potentially active and inactive slip systems are classified as

$$\dot{\gamma}^{(\alpha)} \geq 0, \quad \text{for} f^{(\alpha)} = 0 \ \text{ and } \ \dot{f}^{(\alpha)} = 0, \tag{7a}$$

$$\dot{\gamma}^{(\alpha)} = 0, \quad \text{for} f^{(\alpha)} < 0, \ \text{ or } \ f^{(\alpha)} = 0 \ \text{ and } \ \dot{f}^{(\alpha)} < 0. \tag{7b}$$

Evolution of a resolved shear stress and slip resistance are written as

$$\dot{\tau}^{(\alpha)} = \mathbf{p}^{(\alpha)} : \mathbf{C}^{\mathrm{e}} : \dot{\boldsymbol{\varepsilon}} - \sum_{\beta} \dot{\gamma}^{(\beta)} \mathbf{p}^{(\alpha)} : \mathbf{C}^{\mathrm{e}} : \mathbf{p}^{(\beta)}, \tag{8}$$

$$\dot{g}^{(\alpha)} = \sum_{\beta} h^{(\alpha\beta)} |\dot{\gamma}^{(\beta)}|, \quad h^{(\alpha\beta)} = h_0 \left(1 + \frac{h_0 \gamma_{\mathrm{a}}}{\tau_0 n}\right)^{n-1},$$

$$\gamma_{\mathrm{a}} = \int_0^t \sum_{\alpha} |\dot{\gamma}^{(\alpha)}| \mathrm{d}t, \tag{9}$$

where $\mathbf{s}^{(\alpha)}$ and $\mathbf{m}^{(\alpha)}$ are assumed to be constant, $h^{(\alpha\beta)}$ denotes hardening moduli and τ_0, h_0 and n are material parameters. In Eq. $(9)_2$, the latent hardening is neglected.

From the consistency condition of the yield function, the slip rates, $\dot{\gamma}^{(\alpha)}$, on the active slip systems are determined as

$$\dot{f}^{(\alpha)} = R^{(\alpha)} - \sum_{\beta} X^{(\alpha\beta)} \dot{\gamma}^{(\beta)} = 0, \tag{10}$$

$$\dot{\gamma}^{(\alpha)} = \sum_{\beta} Y^{(\alpha\beta)} R^{(\beta)}, \tag{11}$$

where

$$R^{(\alpha)} := sgn(\tau^{(\alpha)}) \mathbf{p}^{(\alpha)} : \mathbf{C}^{\mathrm{e}} : \dot{\boldsymbol{\varepsilon}}, \tag{12a}$$

$$X^{(\alpha\beta)} := h^{(\alpha\beta)} + sgn(\tau^{(\alpha)}) sgn(\tau^{(\beta)}) \mathbf{p}^{(\alpha)} : \mathbf{C}^{\mathrm{e}} : \mathbf{p}^{(\beta)}, \tag{12b}$$

$$[Y^{(\alpha\beta)}] = [X^{(\alpha\beta)}]^{-1}, \tag{12c}$$

where $(\cdot)^{-1}$ denotes the inverse. Depending on $h^{(\alpha\beta)}$, $X^{(\alpha\beta)}$ may become singular. In that case, slip systems equal to or less than five linearly independent slip systems are selected as active systems from a set of potential slip systems and the other potentially active slip systems are taken to be inactive. The set of potentially active slip systems will be known from Eq. (7). In this computation, isotropic hardening of slip systems is assumed and texture evolution is neglected so that the selection of active slip systems has little influence on the predictions.

We finally obtain the rate-form of the constitutive equation, $\dot{\boldsymbol{\sigma}} = \mathbf{L} : \dot{\boldsymbol{\varepsilon}}$,

$$\mathbf{L} := \mathbf{C}^{\mathrm{e}} - \sum_{\alpha} \left\{ (sgn(\tau^{(\alpha)}) \mathbf{C}^{\mathrm{e}} : \mathbf{p}^{(\alpha)}) \otimes \sum_{\beta} (sgn(\tau^{(\beta)}) Y^{(\alpha\beta)} \mathbf{p}^{(\beta)} : \mathbf{C}^{\mathrm{e}}) \right\}. \tag{13}$$

2.2. Incremental self-consistent model

The incremental self-consistent model proposed by Hill [11], which is widely used for elastoplastic polycrystal, is adopted. With the assumption of equiaxed grains randomly distributed, the polycrystal is considered to consist of spherical phases with a given crystalline orientation. In the self-consistent approach, each constitutive spherical phase is assumed to be embedded in an infinite linear comparison homogenous medium which has a unique tangent moduli corresponding to the effective tangent ones. The phase

average stress and strain rates can be related to the macroscopic ones through the localization tensors, $\mathbf{A}^r$ and $\mathbf{B}^r$,

$$\langle\dot{\boldsymbol{\varepsilon}}\rangle^r = \mathbf{A}^r : \dot{\bar{\boldsymbol{\varepsilon}}}, \quad \langle\dot{\boldsymbol{\sigma}}\rangle^r = \mathbf{B}^r : \dot{\bar{\boldsymbol{\sigma}}}, \tag{14}$$

where the superscript r refers to the quantity for the rth phase, a bar indicates a macroscopic value and $\langle\cdot\rangle$ stands for a volume average. Macroscopic plastic strain rate and equivalent plastic strain are given by

$$\dot{\bar{\boldsymbol{\varepsilon}}}^{\mathrm{p}} = \langle \mathbf{B}^{\mathrm{T}}(\mathbf{x}) : \dot{\boldsymbol{\varepsilon}}^{\mathrm{p}}(\mathbf{x})\rangle, \tag{15}$$

$$\bar{\varepsilon}_{\mathrm{eq}} = \int_0^t \sqrt{(2/3)\dot{\bar{\boldsymbol{\varepsilon}}}^{\mathrm{p}} : \dot{\bar{\boldsymbol{\varepsilon}}}^{\mathrm{p}}}\,\mathrm{d}t, \tag{16}$$

where a superscript T stands for transpose. The rate-form constitutive equation is used to represent linear relationship between the stress and strain rates. The constitutive equations of a phase and effective medium are respectively denoted as

$$\langle\dot{\boldsymbol{\sigma}}\rangle^r = \mathbf{L}^r : \langle\dot{\boldsymbol{\varepsilon}}\rangle^r, \tag{17}$$

$$\dot{\bar{\boldsymbol{\sigma}}} = \tilde{\mathbf{L}} : \dot{\bar{\boldsymbol{\varepsilon}}}, \tag{18}$$

with

$$\tilde{\mathbf{L}} = \langle \mathbf{L}^r : \mathbf{A}^r\rangle, \tag{19}$$

where $\mathbf{L}^r$ and $\tilde{\mathbf{L}}$ are the tangent moduli of a phase and effective medium, respectively. $\mathbf{L}^r$ is assumed to be homogeneous within a phase and can be calculated by Eq. (13) replacing the local quantities with the phase average ones, for instance, a resolved shear stress $\langle\tau^{(\alpha)}\rangle^r = \mathbf{p}^{(\alpha)} : \langle\boldsymbol{\sigma}\rangle^r$ is used instead of $\tau^{(\alpha)} = \mathbf{p}^{(\alpha)} : \boldsymbol{\sigma}$. The strain localization tensor is given by

$$\mathbf{A}^r = \{\mathbf{1} + \mathbf{P} : (\mathbf{L}^r - \tilde{\mathbf{L}})\}^{-1}. \tag{20}$$

where $\mathbf{1}$ is a fourth-order identity tensor and $\mathbf{P}$ is so called Hill's tensor described as

$$\mathbf{P} = \int_{\Omega} \boldsymbol{\Gamma}\,\mathrm{d}V, \tag{21}$$

where

$$\Gamma_{ijkl} = \tfrac{1}{4}(K_{ik}^{-1}\xi_j\xi_l + K_{jk}^{-1}\xi_i\xi_l + K_{il}^{-1}\xi_j\xi_k + K_{jl}^{-1}\xi_i\xi_k), \tag{22a}$$

$$\mathbf{K} = \boldsymbol{\xi}\cdot\tilde{\mathbf{L}}\cdot\boldsymbol{\xi}, \tag{22b}$$

where Ω is the domain within the rth phase and $\boldsymbol{\xi}$ is a position vector on the surface of a phase (see, for instance, [14]). This set of relations defines a nonlinear systems for the average strain rates per phase, $\langle\dot{\boldsymbol{\varepsilon}}\rangle^r$, which can be solved using a fixed-point iterative algorithm.

3. Material parameters and two-stage loading paths

3.1. Material parameters for single- and dual-phase steels

The incremental self-consistent model and rate-independent crystal plasticity theory described in the previous section are used to estimate the mechanical behavior of 600 MPa grade dual-phase steel consisting of ferrite and martensite. In the simulation, both ferrite and martensite are represented by 216 spherical phases with random crystalline orientations and are assumed to have 24 slip systems ($\{1\,1\,0\}\langle 1\,1\,1\rangle$ and $\{1\,1\,2\}\langle 1\,1\,1\rangle$). The volume fractions of ferrite and martensite are 90% and 10%, respectively. Since it is difficult to conduct mechanical test, such as uniaxial tensile test, to identify material parameters in the hardening law only for ferrite (or martensite), they are identified so that simulation reproduces an experimental stress–strain relationship for a 600 MPa grade dual-phase steel. The determined material parameters are shown in Table 1 and a stress–strain curve simulated by the model is depicted in Fig. 1 with an experimental curve. The prediction agrees with the experimental data. However, it is noted that these material parameters are not a unique set of parameters for the dual-phase steel, and alternative sets of material parameters which gives almost the same stress–strain curve would exist.

Table 1
Material parameters for dual-phase steel composing of ferrite and martensite and single-phase steel.

	τ_0 (MPa)	h_0 (MPa)	n	E (GPa)	ν
Ferrite	135	1835	0.15	210	1/3
Martensite	950	1122000	0.03	210	1/3
Single phase	140	5500	0.15	210	1/3

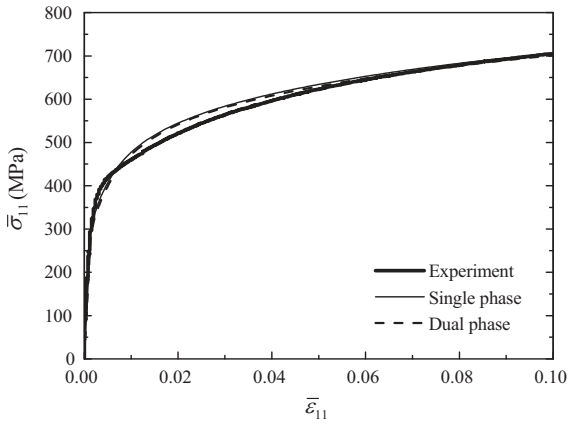

Fig. 1. Comparison of stress–strain curves predicted for single- and dual-phase steels with experimental result.

For comparison purpose, a fictitious single-phase steel which has the same strength as the dual-phase steel is also considered. The single-phase steel is represented by the same number of phases and slip systems as the dual-phase steel, i.e. 216 phases with the 24 slip systems. The material parameters for this polycrystal are listed in Table 1 and the predicted stress–strain curve is shown in Fig. 1. The stress–strain relationship of the single-phase steel is in agreement with that of the dual-phase steel and experiment.

3.2. Two-stage loading paths

In this study, the single- and dual-phase steels are subjected to a two-stage loading path. Uniaxial tension is first applied to a material element in the x_1-direction until $\bar{\varepsilon}_{11}$ reaches 0.03 and the material is fully unloaded (i.e. $\bar{\boldsymbol{\sigma}} = \mathbf{0}$). It is rotated by an angle θ about the x_3-axis and then subjected to uniaxial tension or compression in the x_1-direction until $\bar{\varepsilon}_{\mathrm{eq}}$ reaches 0.08. Hereafter, these three loading stages are called as the pre-loading, unloading and subsequent loading stages. When $\theta = 55^\circ$, the loading path is almost orthogonal loading, that is, the inner product of incremental strain in the pre-loading and subsequent loading stages is about zero.

4. Results for single-phase steel

4.1. Stress–strain curves for two-stage loading paths

First, an investigation is carried out for the single-phase steel to make clear the heterogeneity of stress and strain in the polycrystal and its influence on the work-hardening. The specific influence of the hard martensite phase on the heterogeneity inside the material as well as its work-hardening behavior is further studied in the next section. Fig. 2 shows stress–strain relationships of the single-phase steel under the two-stage loading paths denoted in Section

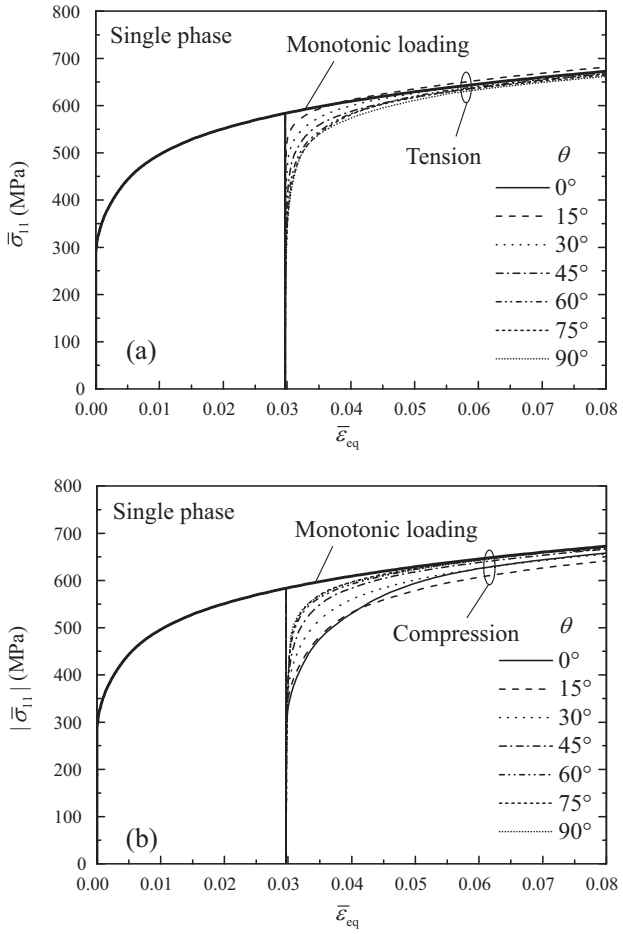

Fig. 2. Macroscopic stress–strain curve of single phase polycrystal under uniaxial tension followed by (a) uniaxial tension and (b) uniaxial compression.

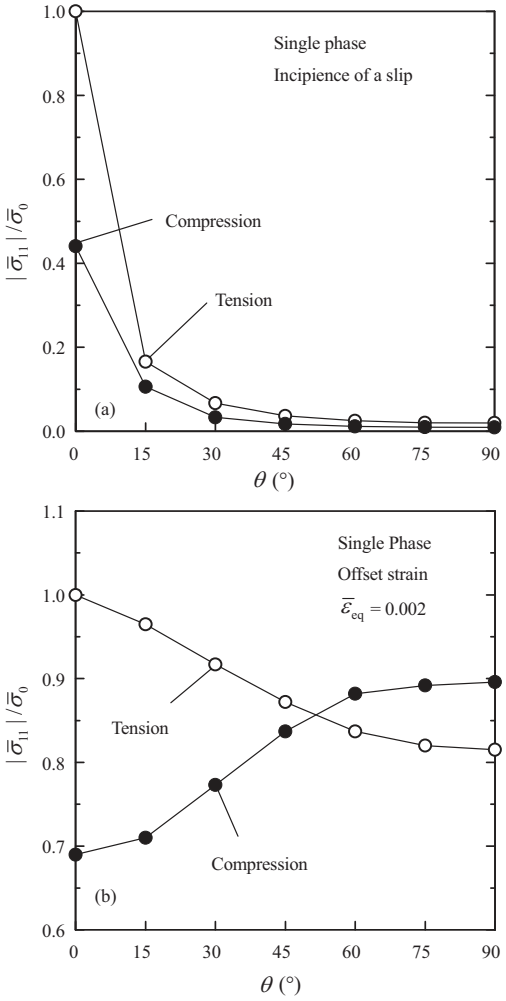

Fig. 3. Orientation dependence of re-yield stress evaluated at (a) incipience of a slip and (b) 0.2% accumulation of macroscopic equivalent plastic strain. Re-yield stress is normalized by one for $\theta = 0^\circ$ with uniaxial tension in subsequent loading stage, which is denoted by $\bar{\sigma}_0$.

3.2. The stress–strain curve for the monotonic uniaxial tension is also depicted in the figure as a reference. When the material is subjected to the uniaxial tension in the subsequent loading with $\theta = 0^\circ$, the re-yield stress is identical to the stress state before unloading and the subsequent flow stress corresponds to the one under the monotonic loading, since the material deforms elastically during unloading. For the other loading paths, the plastic deformation takes place at a stress level which is lower than the flow stress before unloading. Namely, a cross-softening behavior is predicted for each change of loading paths. Macroscopic stress at re-yielding is evaluated quantitatively by using two definitions: (i) the stress state at incipience of a slip (i.e. microplastic yield) and (ii) 0.2% proof stress determined by means of a conventional offset-strain method (i.e. macroplastic yield). The re-yield stress is shown in Fig. 3 as a function of θ. The re-yield stress is normalized by the one, denoted by $\bar{\sigma}_0$, for the uniaxial tension with $\theta = 0^\circ$. When uniaxial tension is applied subsequently, the re-yield stress determined by the incipient of a slip (microplastic yield) decreases drastically with increasing the rotation angle θ. Indeed, $|\bar{\sigma}_{11}|/\bar{\sigma}_0$ becomes less than 0.1 for $\theta \geq 30^\circ$. The same trend is predicted when the uniaxial compression is applied in the subsequent loading stage. On the other hand, the re-yield stress determined as the 0.2% proof stress (macroplastic yield) shows different types of orientation dependence in tension and compression. For the uniaxial tension, the 0.2% proof stress decreases with increasing θ, whereas it increases when the subsequent loading is uniaxial compression. The normalized 0.2% proof stress is the lowest for the compression with $\theta = 0^\circ$, and the so called Bauschinger effect is predicted to appear for this material. After re-yielding the flow stress grows approaching to the reference monotonic loading curve. Thus, the orientation dependence of flow stress weakens with the plastic deformation. At $\bar{\varepsilon}_{eq} = 0.08$, deviations of the flow stress from the reference curve are within −1.6% to 1.3% when the uniaxial tension is applied in the subsequent loading and within −4.7% to −0.2% when the uniaxial compression is applied.

From these computations, it is found on one hand that the strain-path change causes the Bauschinger effect as well as the orientation dependent transitional re-yielding behavior. On the other hand, the degree of path-dependence weakens with the plastic deformation. In the following sections, our investigation will be devoted to clarify the mechanisms for the transitional re-yielding behavior, especially, the ones causing (i) the Bauschinger effect for $\theta = 0^\circ$, (ii) the orientation dependence of the stress for incipient slip (microplastic yield), and (iii) the orientation dependence of the 0.2% proof stress (macroplastic yield).

4.2. Resolved shear stress before and after unloading stage

To understand the mechanism behind the Bauschinger effect, the resolved shear stress on slip systems, which plays an essential role in crystal plasticity model, is examined. Hereafter, the resolved shear stress is simply denoted by RSS. RSS before and after

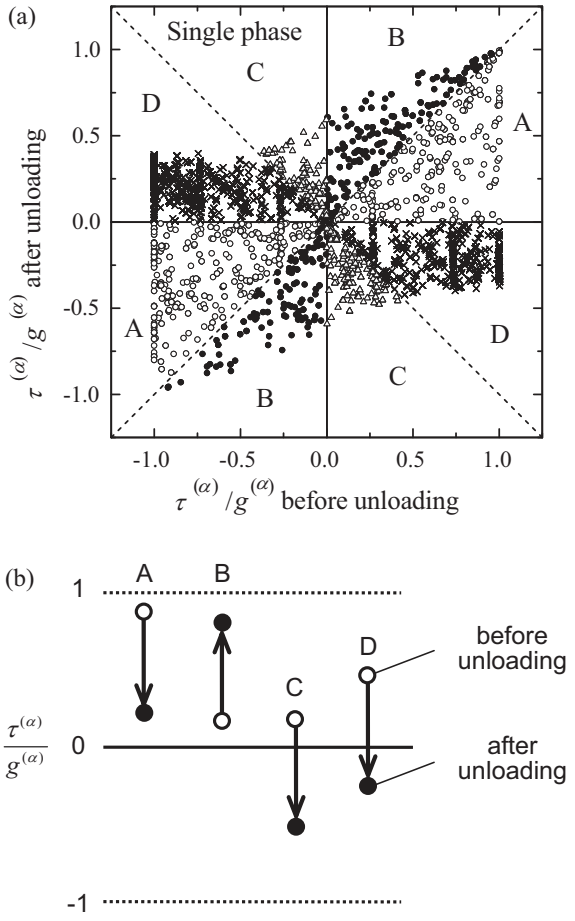

Fig. 4. Change of resolved shear stress, $\tau^{(\alpha)}$, before and after unloading stage. Resolved stress is normalized by corresponding slip resistance, $g^{(\alpha)}$. (a) Scatter diagram and (b) schematic illustration of change of $\tau^{(\alpha)}$ in the first and fourth quadrants in (a).

unloading is shown in Fig. 4(a), where RSS is normalized by its slip resistance, $\tau^{(\alpha)}/g^{(\alpha)}$. In the figure, the plots are classified into four groups, A, B, C and D, and different marks are used for the data belonging in each group. The changes of RSS in the first and fourth quadrants are schematically illustrated in Fig. 4(b) (Note that the reasoning is the same for the second and third quadrants with RSS having opposite signs). The RSS in the group A is changed such that the absolute value is decreased during unloading stage with keeping its sign the same. For the group B, the absolute value of RSS is increased without the change of the sign, hence the RSS approaches to the slip resistance. For the group C, the absolute value of RSS is increased with changing the sign. The RSS becomes close to the slip resistance (yield stress) in the opposite direction. For the group D, the absolute value of RSS is decreased with the change of the sign, and the absolute values of RSS become smaller after unloading. Thus, the macroscopic unloading leads to unloading, in the sense that the absolute value of RSS decreases, for the groups A and D, on the contrary, for the groups B and C, the RSS becomes closer to the slip resistance due to macroscopic unloading. In fact, 26% of the data belongs in the groups B and C. Concerning the reversed subsequent loading stage (Bauschinger loading), the variation of the applied macroscopic stress follows the one during unloading, so that the RSS changes in the same way as shown in Fig. 4(b). Consequently, the RSS in the groups B and C reaches the slip resistance earlier, and therefore the Bauschinger effect occurs.

From Fig. 4, it has become clear that the RSS is neither zero nor uniform after unloading, besides, its magnitude becomes higher for some slip systems during the macroscopic unloading stage. As a result, the Bauschinger effect appears within the polycrystal. It is recalled that in the present case an isotropic hardening at the slip system scale has been considered.

4.3. Change of resolved shear stress due to uniaxial stress increment/decrement

In this section, the investigation on the RSS proceeds further to elucidate the mechanism for the orientation dependence of the transitional re-yielding behavior. Re-yielding can occur at lower macroscopic stress level if the large residual RSS exist after unloading, since small stress increment is required for re-yielding. However, even if the residual RSS is small, re-yield is possible to occur at lower stress level as long as the RSS changes notably during the subsequent loading. Thus, the magnitude of RSS after unloading (cf. Fig. 4) as well as the degree of change of the RSS in the subsequent loading are the two main parameters to describe the re-yielding behavior. In the subsequent loading stage, all phases undergo uniaxial stress increment/decrement, because of the assumed elastic isotropy, until a phase begins to yield (note however that the stress state is not uniaxial because of the residual stress state). After yielding, no phase is subjected to exact uniaxial stress increment/decrement. However, since the focus is on the incipient re-yielding state, the assumption that all phases undergo uniaxial tension is a reasonable approximation. Before a slip system activates, the change of the RSS, $\Delta\tau^{(\alpha)}$, on the slip system due to the uniaxial stress increment/decrement, $\Delta\bar{\sigma}_{11}$, is given by $\Delta\tau^{(\alpha)} = s_1^{(\alpha)}\Delta\bar{\sigma}_{11}m_1^{(\alpha)}$. The change of the normalized RSS $\Delta\tau^{(\alpha)}/\Delta\bar{\sigma}_{11}$ (i.e. the Schmid factor for a given slip system) for $\theta = 0^\circ$ and 90° is shown in Fig. 5(a) and (b) as a function of $\tau^{(\alpha)}/g^{(\alpha)}$ after unloading. The classification of the data into A, B, C and D corresponds to the one used in Fig. 4. For $\theta = 0^\circ$ (Fig. 5(a)), the slip systems with an absolute value of $\tau^{(\alpha)}/g^{(\alpha)}$ close to 1 presents a Schmid factor $\Delta\tau^{(\alpha)}/\Delta\bar{\sigma}_{11}$ which is almost zero. This can be explained by the fact that during uniaxial tension in the pre-loading stage, a multiaxial stress state is created because of the plastic anisotropy of the crystals. During the unloading stage, only tensile stress component decreases for all phases and the RSS can be hardly changed for the slip systems with a Schmid factor close to zero, and consequently $|\tau^{(\alpha)}|/g^{(\alpha)}$ stays about one.

On the other hand, for $\theta = 90^\circ$ (Fig. 5(b)), the width of the distribution of $\Delta\tau^{(\alpha)}/\Delta\bar{\sigma}_{11}$ is almost constant for any $\tau^{(\alpha)}/g^{(\alpha)}$ after unloading. This difference arises from the rotation of the subsequent loading, which changes the orientation of slip systems ($\mathbf{s}^{(\alpha)}$ and $\mathbf{m}^{(\alpha)}$) with respect to the loading direction (the x_1-direction) while the RSS remains constant. For $\theta = 90^\circ$, the slip system where $|\tau^{(\alpha)}|/g^{(\alpha)} \approx 1$ and $\Delta\tau^{(\alpha)}/\Delta\bar{\sigma}_{11}$ is large activates first with a small stress increment in the subsequent loading. The macroscopic stress required to activate this slip system is obviously smaller than the one required to activate any slip systems for $\theta = 0^\circ$. The relationship between $\Delta\tau^{(\alpha)}/\Delta\bar{\sigma}_{11}$ and $|\tau^{(\alpha)}|/g^{(\alpha)}$ after unloading has been checked for the other rotation angles and it has been found that the trend of the distribution of $\Delta\tau^{(\alpha)}/\Delta\bar{\sigma}_{11}$ varies continuously from the case for $\theta = 0^\circ$ to 90°. Therefore, the larger θ is, the smaller the macroscopic stress required to cause a slip becomes. This explains the orientation dependence of the incipience of the plastic slip as shown in Fig. 3. When the subsequent loading is uniaxial stress decrement, the distribution of $\Delta\tau^{(\alpha)}/\Delta\bar{\sigma}_{11}$ remains the same. Therefore, the stress state at the incipience of re-yielding becomes also lower with increasing θ.

The macroscopic stress at the incipience of a slip is governed by the lowest macroscopic stress increment that activates one slip system, on the contrary, numerous slip systems have already been activated within the polycrystal when the offset strain is 0.2%. To study the 0.2% proof stress, all data points in Fig. 5(a) and (b) are

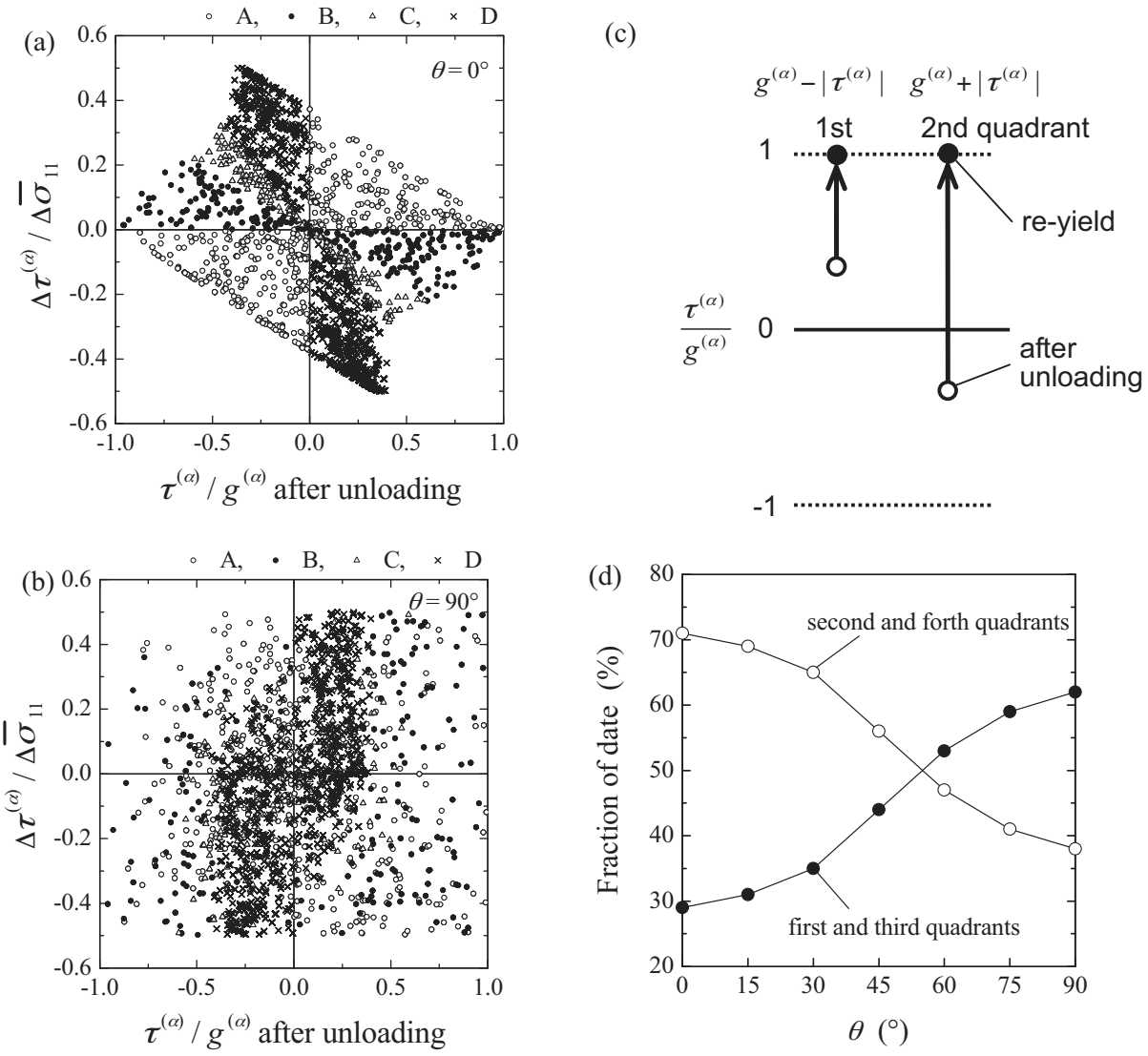

Fig. 5. Change of resolved shear stress due to uniaxial stress increment for (a) $\theta = 0^\circ$ and (b) $\theta = 90^\circ$ ($\Delta\tau^{(\alpha)}/\Delta\bar{\sigma}_{11}$ corresponds to the Schmid factor for a slip system), (c) a distance of stress between unloaded state and re-yield state, and (d) fraction of data belonging to the first and third quadrants and the second and forth quadrants in (a), (b) and figures for other θ.

considered. Firstly, let us examine the case that $\Delta\bar{\sigma}_{11}$ is positive, which corresponds to the macroscopic uniaxial tension in the subsequent loading stage. For the data in the first and third quadrants, the RSS after unloading and $\Delta\tau^{(\alpha)}$ have the same sign, therefore the change of RSS required for re-yielding is $g^{(\alpha)} - |\tau^{(\alpha)}|$. This is illustrated in Fig. 5(c). On the other hand, the RSS and $\Delta\tau^{(\alpha)}$ in the second and fourth quadrants have the opposite sign, and an increment of $g^{(\alpha)} + |\tau^{(\alpha)}|$ is accordingly required for re-yielding. Consequently, the slip system belonging to the second and fourth quadrants require a higher stress increment to yield than those in the first and third quadrants. Thus, it is expected that the 0.2% proof stress becomes lower when less data on the slip systems belong to the second and fourth quadrants. For each θ, the data belonging to each quadrant have been calculated and the result is shown in Fig. 5(d). The fraction of the data in the second and fourth quadrants decrease with increasing θ. This implies that the 0.2% proof stress decreases with increasing θ. A good correlation is thus obtained with the orientation dependence of 0.2% proof stress shown in Fig. 3(b).

Next, we consider the case with negative $\Delta\bar{\sigma}_{11}$, which is analogous to the macroscopic uniaxial compression in the subsequent loading stage. Then, the sign of $\Delta\tau^{(\alpha)}$ becomes opposite without any influence on the distribution of data in Fig. 5(a) and (b). Namely, $\Delta\tau^{(\alpha)}$ is negative in the first and second quadrants and is positive in the third and fourth quadrants. Due to this change, the relationship discussed above, accordingly, becomes opposite. Thus, the 0.2% proof stress becomes lower when less data belong in the first and third quadrants. The fraction of the data in the first and third quadrants shown in Fig. 5(d) is consistent with the orientation dependence of the 0.2% stress.

In this subsection, the mechanism behind the orientation dependence of the re-yield behavior has been investigated in terms of the magnitude of the RSS after unloading and the degree of the change of RSS due to the uniaxial stress increment/decrement (geometrical Schmid factor). The rotation of the subsequent loading path, which changes the relationship between the slip systems, described by $\mathbf{s}^{(\alpha)}$ and $\mathbf{m}^{(\alpha)}$, and the loading direction leads to the orientation dependence of the re-yielding behavior. Based on the knowledge obtained for single-phase polycrystals, the investigation is extended to the work-hardening behavior of the dual-phase steel under the two-stage loading paths.

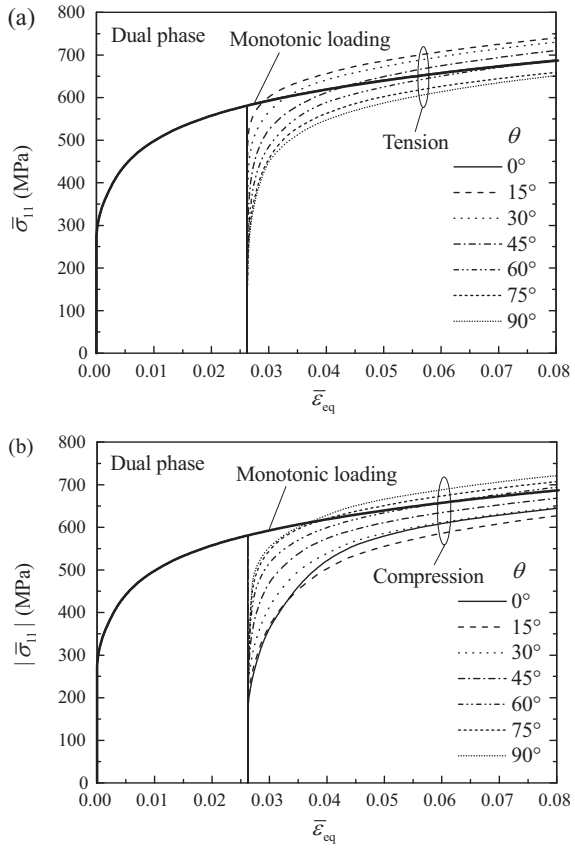

Fig. 6. Macroscopic stress–strain curve of dual-phase steel under uniaxial tension followed by (a) uniaxial tension and (b) uniaxial compression.

5. Results for dual-phase steel

5.1. Stress–strain relationship for dual-phase steel

In this section our investigation is extended to the dual-phase steel described in Section 3.1 by comparison with the mechanical behavior of single-phase steel. Stress–strain relationships of the dual-phase steel estimated under the two-stage loading paths, which are the same as the ones prescribed for the single-phase steel, are shown in Fig. 6. The transient re-yielding behavior, which has been observed for the single-phase steel, is also predicted for the dual-phase steel. For the quantitative assessment, 0.2% proof stress is determined by using the offset-strain method employed in the previous section, and the result is shown in Fig. 7. The dual-phase steel possesses the same trend in the orientation dependence of 0.2% proof stress as the single-phase steel. The decrease of the re-yield stress is, however, more significant for the dual-phase steel, thus, the orientation dependence of the 0.2% proof stress is more pronounced due to the existence of the hard martensite. After re-yielding the flow stress becomes higher or lower than the reference stress–strain curve under the monotonic loading depending on the rotation angle, θ. The flow stresses do not asymptotically approach to the reference curve, at least in the strain range considered in this study, unlike the single-phase steel case. The deviation from the reference curve is within −5.1% to 7.8% when the uniaxial tension is applied in the subsequent loading and within −8.7% to 5.1% when the uniaxial compression is applied.

In the following sections, the mechanisms being responsible for (i) the enhancement of orientation dependence of 0.2% proof stress and (ii) the deviation of the flow stress from the reference curve is investigated in details.

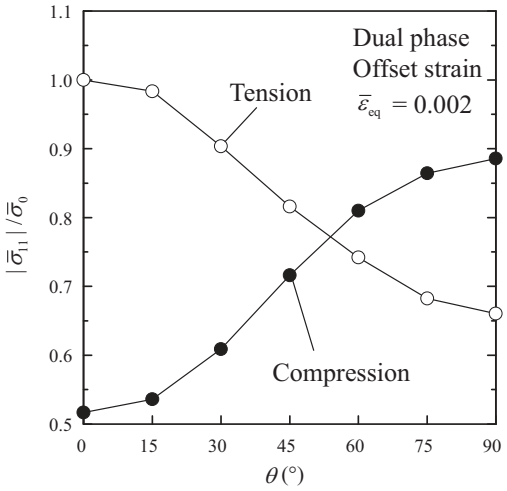

Fig. 7. Orientation dependence of re-yield stress evaluated as 0.2% proof stress, normalized by the one for uniaxial tension with $\theta = 0^\circ$, denoted by $\bar{\sigma}_0$.

5.2. Resolved shear stress of slip systems in ferrite

Since the orientation dependence of the re-yield behavior is qualitatively the same for the single- and dual-phase steels, the behavior observed for the dual-phase steel can be explained by applying the same approach used in the previous section, i.e. the examination of the RSS. Because the martensite deforms elastically during the pre-loading and unloading stages, the RSS before and after unloading are only shown for the ferrite phase (Fig. 8). It can be observed that the area where the data of RSS is plotted is stretched into the positive and negative vertical directions in the figure with respective to the one for the single-phase steel. This extension of the plotted area means that the residual RSS in the ferrite is higher than that for the single-phase steel. Thus, the martensite enhances the residual RSS in ferrite. Before unloading, the macroscopic tensile stress and the average tensile stresses for ferrite and martensite are 580 MPa, 532 MPa and 1019 MPa, respectively. Since the same elastic properties are assigned for all phases, these stresses decrease equally by an amount of 580 MPa during unloading and consequently become 0 MPa, −48 MPa and 437 MPa, respectively. On the other hand, for the single-phase steel, the average stress is, of course, 0 MPa, since the macroscopic stress is identical to the average stress in this case. From the viewpoint of average stress, the

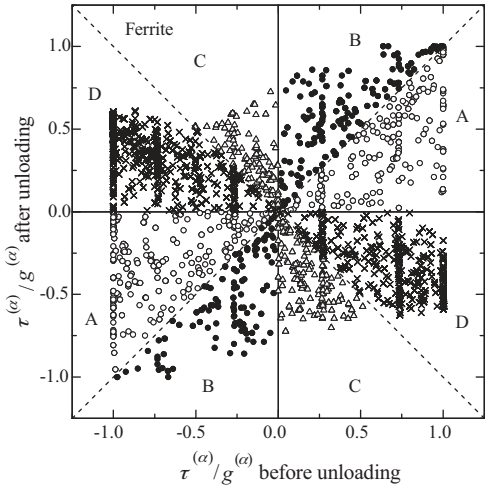

Fig. 8. Change of resolved shear stress, $\tau^{(\alpha)}$, before and after unloading for ferrite. $\tau^{(\alpha)}$ is normalized by slip resistance, $g^{(\alpha)}$.

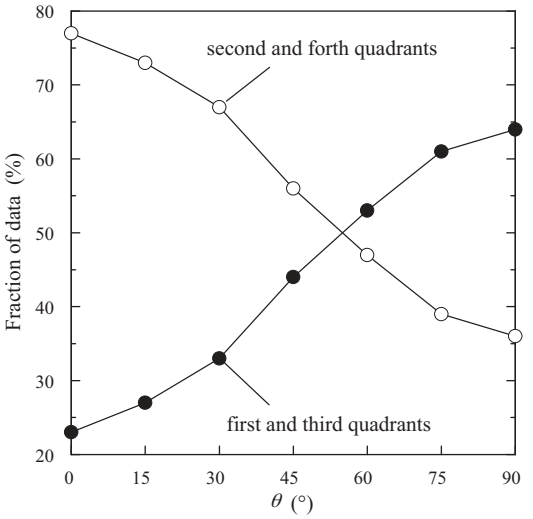

Fig. 9. Fraction of data belonging in the first and third quadrants and the second and forth quadrants in figure showing relationship between $\Delta\tau^{(\alpha)}/\Delta\bar{\sigma}_{11}$ and $\tau^{(\alpha)}/g^{(\alpha)}$ after unloading.

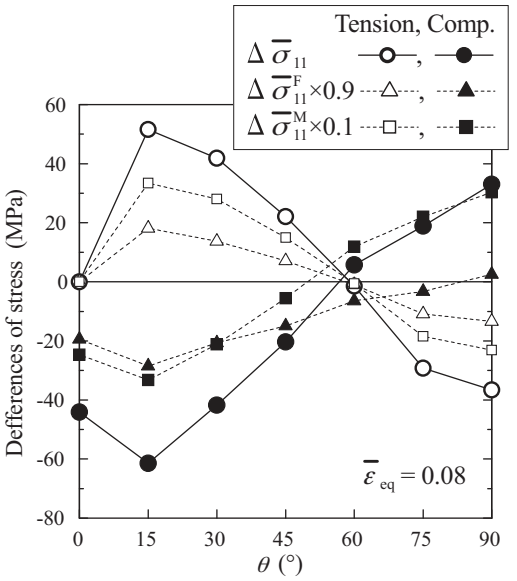

Fig. 10. Deviation of macroscopic tensile stress for two-stage loading paths from that for monotonic loading is decomposed into average stresses of ferrite and martensite.

ferrite is more loaded in inverse direction after unloading. Thus, the residual RSS becomes higher when the hard martensite is present. In Fig. 8, the mapped area of B, C, and D are especially expanded, while the area for A does not changed. As shown in Fig. 4(b), the RSS after unloading in the groups B and C play an important role for the Bauschinger effect. When the RSS in the groups B and C are high, the Bauschinger effect is pronounced. This explains the reason why the Bauschinger effect and the orientation dependence of the 0.2% proof stress are enhanced for the dual-phase steel.

The change of the RSS, $\Delta\tau^{(\alpha)}$, due to the uniaxial stress increment/decrement, $\Delta\bar{\sigma}_{11}$, is calculated for the ferrite by using the same method adopted in the previous section. The distribution of the data is similar to the one for the single-phase steel, since the calculated shear stress increment, $\Delta\tau^{(\alpha)} = s_1^{(\alpha)}\Delta\bar{\sigma}_{11}m_1^{(\alpha)}$, is the same for each slip systems. Difference is derived only from the increase of $\tau^{(\alpha)}/g^{(\alpha)}$ after unloading. For the figure showing the relationship between $\Delta\tau^{(\alpha)}/\Delta\bar{\sigma}_{11}$ and $\tau^{(\alpha)}/g^{(\alpha)}$ after unloading, the fraction of the data mapped in each quadrant has been calculated. The result is shown in Fig. 9. The figure shows the same trend than the one observed for the single-phase steel, and the variation of the fraction is enhanced for the ferrite in the dual-phase steel. This is consistent with the observation that the same orientation dependence is predicted for the single- and dual-phase steels and the magnitude of the orientation dependence is more pronounced for the dual-phase steel.

5.3. Localization of stress and strain in martensite

In this section, the mechanism for the increase and decrease of the flow stress after re-yielding is investigated. The macroscopic stress is given by the sum of the average stresses in the ferrite and martensite multiplied by the volume fractions: $\bar{\boldsymbol{\sigma}} = 0.9\langle\boldsymbol{\sigma}\rangle^{\mathrm{F}} + 0.1\langle\boldsymbol{\sigma}\rangle^{\mathrm{M}}$. The deviation of the flow stresses in the two-stage loading paths from that for the monotonic loading is calculated for the macroscopic stress and average stresses in the ferrite and martensite at $\bar{\varepsilon}_{\mathrm{eq}} = 0.08$. The results are shown in Fig. 10. The summation of the deviations in the average stresses of ferrite and martensite are identical to that in the macroscopic stress. The absolute value of the flow stress is compared when the subsequent loading is the uniaxial compression. Deviation of flow stress appears for the average stresses in both ferrite and martensite, and the deviation of the average stress of martensite contributes to the deviation of the macroscopic stress for most of the loading paths. The development of stress and strain states in the martensite will be examined first and then those in ferrite. In the series of computation, the martensite stays in elastic regime during the pre-loading and unloading stages. In the subsequent loading stage, it remains in the elastic regime for the case that the uniaxial tension is applied with $\theta = 0^\circ$, 60°, 75° and 90° and the uniaxial compression is applied with $\theta = 60^\circ$, 75° and 90°. For the other loading paths, the martensite remains in the elastic regime until $\bar{\varepsilon}_{\mathrm{eq}}$ reaches 0.042 and the plastic deformation begins to grow after this strain level. The average equivalent plastic strain in the martensite is less than 0.004 at $\bar{\varepsilon}_{\mathrm{eq}} = 0.08$. For half of the loading paths, no plastic deformation takes place and the elastic behavior of each phase is the same, so that the stress and strain are the same for all martensite crystalline phases. Because of this, the investigation can be made on the average stress and strains rather than the RSS for each phase. Developments of the average tensile stress in martensite, $\langle\sigma_{11}\rangle^{\mathrm{M}}$, is shown in Fig. 11. The dot in the figure indicates the stress state after rotation (just before subsequent loading). Since the material element is rotated about the x_3-axis, $\langle\sigma_{11}\rangle^{\mathrm{M}}$ varies with θ. The development of stress is rapid at the beginning of subsequent loading stage and then becomes slow for all loading paths, except for the uniaxial tension with $\theta = 0^\circ$, in which the stresses grow

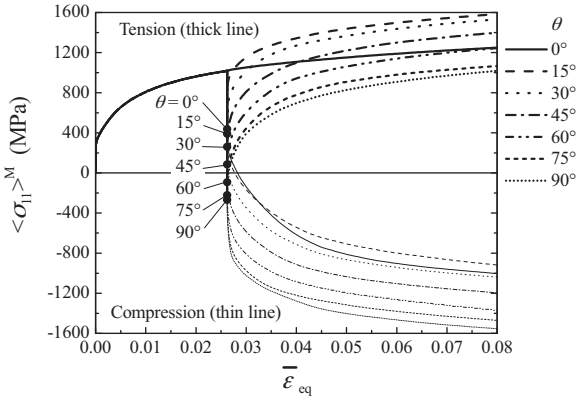

Fig. 11. Development of average tensile stress of martensite.

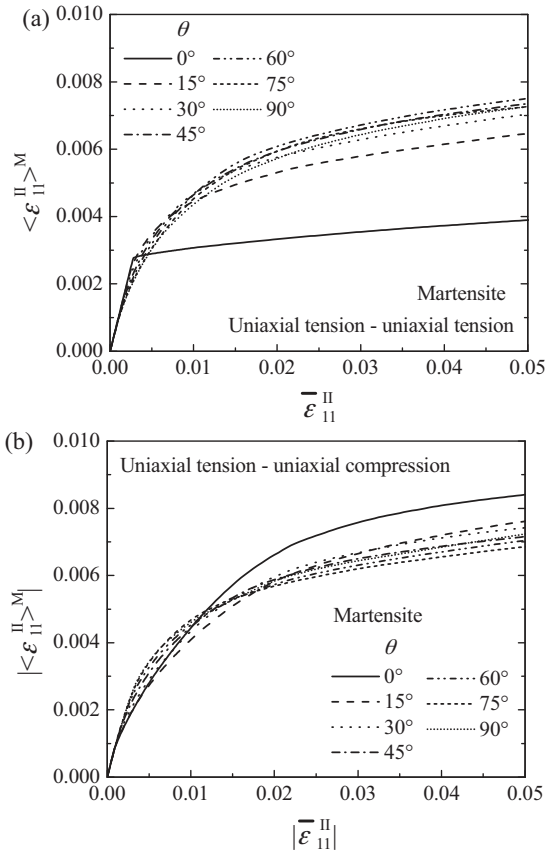

Fig. 12. Development of average strain for martensite as a function of macroscopic strain in subsequent loading stage.

more slowly. The stresses in martensite grow with almost the same speed. The occurrence of the plastic deformation in the martensite, the amount of which is about 0.004, has little influence on the growth of the average stress. The stresses do not tend to approach to the stress for the monotonic loading, $\theta = 0^\circ$. This behavior is the same as the trend which appears in the macroscopic flow stress in Fig. 6. The difference of stresses between $\theta = 15^\circ$ and 90° is 659 MPa after the rotation, and at $\bar{\varepsilon}_{eq} = 0.08$ it becomes to 565 MPa and 639 MPa for tension and compression, respectively. They are 86% and 97% of the original difference induced by the rotation. Therefore it can be concluded that the difference of stress which appears in the martensite in the subsequent loading stage is mainly due to the change of stress components caused by the rotation of the subsequent loading path.

Only for the uniaxial tension with $\theta = 0^\circ$, the martensite stress grows more slowly than for the other loading paths. The development of the strain for martensite is checked for all loading paths. Macroscopic strain and average strain of the martensite in the subsequent loading, which are respectively denoted by $\bar{\varepsilon}^{II}_{11}$ and $\langle \varepsilon^{II}_{11} \rangle^{M}$, are shown in Fig. 12. Strain localization is less for $\theta = 0^\circ$ than for the other loading paths. This low localization is consistent with the smaller stress growth in Fig. 11 and is relevant with the transitional yielding behavior: for the tension with $\theta = 0^\circ$, some of the ferrite phases enter the plastic regime simultaneously and the gradient of the stress–strain curve (and tangent moduli) of ferrite suddenly decreases, whereas for the other cases the ferrite phases begin to re-yield one by one and the gradient of the stress–strain curve decreases gradually. At the beginning of the subsequent loading the tangent moduli of the ferrite are smaller for $\theta = 0^\circ$ than for the other loading paths, which means the ferrite is weaker for $\theta = 0^\circ$. Therefore, the strain concentration in martensite is weak for $\theta = 0^\circ$ and the growth of flow stress is accordingly less. The transitional re-yielding behavior is responsible for the strong strain localization in the martensite.

The difference of stress state in the martensite, which is the main source of the discrepancy of the macroscopic flow stress, is caused by the change of stress state due to the rotation of the material element as well as the strong strain localization caused by the transitional re-yielding behavior. In the next subsection, the discrepancy of stress in the ferrite is discussed.

5.4. Stress state in ferrite

As is shown in Fig. 10, the average stress in the ferrite for the two-stage loading path also deviates from that for the monotonic loadings. The development of stress in ferrite under the two-stage loading path is compared with that for the monotonic loading path, and it is found that various mechanisms influence the flow stress with the same order of significance. A difference is observed in the amount of the hydrostatic stress depending on the rotation angle. The hydrostatic stress has no influence on the yielding behavior of a crystal, however, the degree of tensile stress depends on the amount of superposed hydrostatic stress. The ratio of the stress deviator also varies with the loading paths. In the ferrite, multiaxial stress state is created and the change of stress ratio makes the amount of tensile stress required for yielding different. For example, concerning to the two-dimensional yield surface of an isotropic polycrystal, the major stress component is higher at stress point corresponding to the plane strain stretching than to the uniaxial tension. From these reasons, the flow stress in the ferrite depends on the loading path.

6. Discussion

In this work, the work-hardening behavior of single- and dual-phase steels have been investigated by means of the incremental self-consistent model with a rate-independent crystal plasticity model. For the dual-phase steel, a strong Bauschinger effect is predicted under the uniaxial tension followed by the uniaxial compression. This behavior is caused by the heterogeneous stress field within the material due to the mechanical contrast of two phases. This is consistent with the numerical results shown by Zhonghua and Haicheng [9] and Terada et al. [10], who adopted the finite element method. In the work of Terada et al. [10], two types of two-phase material, in which fiber- or spherical-types of hard phase are reinforced, are modeled and it was shown that the inhomogeneity of stress/strain field is higher for the fiber-type model and the Bauschinger effect is more significant for this material. This conclusion is consistent with our results, as expected, since the larger Bauschinger effect has been predicted for the dual-phase steel, in which the heterogeneity of the stress field is enhanced with respect to the single-phase steel. From these comparisons, the self-consistent model adopted here, which is more efficient than the finite element model in terms of computational cost, is able to capture the main influence of the heterogeneity features of the local stress field.

Tarigopula et al. [7] observed the work-hardening behavior of a 800 MPa grade dual-phase steel under two-stage loading paths consisting of uniaxial tension, unloading, rotation of material and subsequent uniaxial tension. In the experiment, uniaxial tension was, first, applied to a large specimen in the rolling direction until tensile strain reaches 0.01, 0.04 and 0.08, and after unloading small specimens were cut from it at 0°, 45° and 90° inclined from the rolling direction. It was shown that the re-yield stress becomes low with increasing the rotation angle. This is agreement with our prediction shown in Fig. 6. However, none of their experimental stress–strain curves becomes greater than the one for the mono-

tonic uniaxial tension after re-yielding, which is different from what has been found in the present study. The volume fraction of martensite is 0.3 in their study while it is 0.1 in the present computation. The influence of volume fraction of martensite is still an open question.

7. Summary

In this work, the work hardening behavior of dual-phase as well as single-phase steel has been inferred from a self-consistent micromechanical modeling. Two-stage loading paths consisting of pre-loading, unloading and subsequent loading for various directions have been considered. The Bauschinger effect and the orientation dependent transitional re-yielding behavior have been predicted for both types of polycrystals. It has been found that the resolved shear stresses on some slip systems are raised during macroscopic unloading stage, and this results in the early re-yielding (i.e. Bauschinger effect). The rotation of the subsequent loading changes the orientation of the slip systems with respect to the loading direction as well as the relationship between the RSS after unloading and the direction and amount of the increment of RSS in the subsequent loading. Consequently, the increment of RSS required for the re-yielding on a slip system varies with the rotation angle. This is responsible for the orientation dependent re-yielding behavior. After the beginning of re-yielding the orientation dependence weakens and the flow stress tends to approach the one corresponding to the monotonic loading.

On one hand, for the dual-phase steel, the orientation dependence of re-yielding behavior is more pronounced and the permanent hardening and/or softening is predicted. After unloading, the average stress in the ferrite is negative and the one in martensite is positive. The mechanical contrast of the ferrite and martensite enhances the heterogeneity of the stress field. The negative residual stresses in the ferrite leads to a pronounced Bauschinger effect and the orientation dependent re-yielding behavior. The permanent hardening or softening of flow stress, which is not observed for the single-phase steel, is caused by the change of the stress components in martensite due to the rotation of the material.

In this work, the investigation has been focused on the influence of the heterogeneity of stress/strain field on the work-hardening behavior by neglecting the development of texture and latent hardening of slip systems. These different features of course emerge in the deformation process of a real material and affect the work-hardening behavior. An investigation considering these different topics as well as an experimental validation are the next target of this research.

Acknowledgement

The authors acknowledge Nippon Steel Corporation for a financial support to this study.

References

[1] E.F. Rauch, J.H. Schmitt, Mater. Sci. Eng. A 113 (1989) 441.
[2] S. Thuillier, E.F. Rauch, Acta Metall. Mater. 42 (1994) 1973.
[3] B. Peeters, B. Bacroix, C. Teodosiu, P. Van Houtte, E. Aernoudt, Acta Mater. 46 (2001) 1621.
[4] B. Gardey, S. Bouvier, B. Bacroix, Metall. Mater. Trans. A 36 (2005) 2937.
[5] M.G. Lee, D. Kim, C. Kim, M.L. Wenner, R.H. Wagoner, K. Chung, Int. J. Plast. 21 (2005) 883.
[6] H. Haddadi, S. Bouvier, M. Banu, C. Maier, C. Teodosiu, Int. J. Plast. 22 (2006) 2226.
[7] V. Tarigopula, O.S. Hopperstada, M. Langsetha, A.H. Clausena, Eur. J. Mech. A 27 (2008) 764.
[8] J. Cao, W. Lee, H.S. Cheng, M. Seniw, H.P. Wang, K. Chung, Int. J. Plast. 25 (2009) 942.
[9] L. Zhonghua, G. Haicheng, Metall. Trans. A 21 (1990) 717.
[10] K. Terada, K. Matsui, M. Akiyama, T. Kuboki, Comput. Mater. Sci. 31 (2004) 67.
[11] R. Hill, J. Mech. Phys. Solids 13 (1965) 89.
[12] J.W. Hutchinson, Proc. R. Soc. Lond. A 319 (1970) 247.
[13] K. Yoshida, R. Brenner, B. Bacroix, S. Bouvier, Eur. J. Mech. A 28 (2009) 905.
[14] T. Mura, Micromechanics of Defects in Solids, Martinus Nijhoff Publishers, The Hague, 1982.